RSC Sustainability

ROYAL SOCIETY OF CHEMISTRY

PAPER

View Article Online
View Journal | View Issue

Cite this: *RSC Sustainability*, 2025, **3**, 4677

Recycled electrode-based lithium-ion capacitors: an efficient route for transforming LIB waste into high-performance energy storage devices

Subhajit Bhowmik, Tausif Ahamad Ansari, Madhushri Bhar and Surendra K. Martha *

The rapid proliferation of lithium-ion batteries (LIBs) has amplified concerns, with waste levels predicted to reach 1.1 million tons by 2030. Current recycling efforts predominantly focus on either recovering critical metals such as lithium, nickel, and copper or the direct regeneration of electrode materials. However, a gap exists in fully utilizing these materials to create high-value products while recovering only metals. Besides, direct regeneration involves challenges due to impurities, material degradation, complex separation techniques, and difficulties restoring the original performances. Therefore, this study explores innovative upcycling strategies to efficiently repurpose cathode and anode materials from spent LIBs into lithium-ion capacitors (LICs) through a simplified and effective approach. Herein, mixed cobalt oxide (mCO-R), generated from the spent $LiCoO_2$ and activated graphene oxide (AGO-R), developed from the spent graphite, is utilized as an anode and cathode material for LICs, respectively, after coating onto a carbon fiber (CF) mat. Switching from a Cu current collector to a carbon fiber backbone is crucial in boosting Li-ion storage, accommodating volume changes in the internal void spaces, and providing mechanical stability. The resulting LIC delivers an energy density and power maxima of 206 Wh kg^{-1} and 7560 W kg^{-1}, respectively, rendering 75% retention after prolonged durability of 10 000 cycles. Thus, the approach not only supports a circular economy offering sustainable solutions to mitigate LIB waste but also contributes to the rising demand for renewable energy storage, showcasing the value derived from end-of-life LIBs.

Received 6th June 2025
Accepted 17th August 2025

DOI: 10.1039/d5su00413f

rsc.li/rscsus

Sustainability spotlight

The rapid growth of lithium-ion batteries (LIBs) has led to mounting environmental concerns from spent cells. This work advances sustainability by innovatively repurposing waste LIB materials— $LiCoO_2$ and graphite—into high-performance lithium-ion capacitors (LICs), thus addressing both energy storage needs and electronic waste management. By eliminating metallic current collectors in favor of a 3D carbon fiber framework, the design reduces material intensity and enhances device performance. This circular approach supports UN SDG 7 (affordable and clean energy) by improving access to high-efficiency storage, SDG 12 (responsible consumption and production) through materials reuse, and SDG 13 (climate action) by lowering emissions associated with raw material extraction and battery waste disposal. The work exemplifies sustainable innovation for a cleaner energy future.

1 Introduction

The rapid adoption of lithium-ion batteries (LIBs) over the last two decades has led to significant growth in their versatile applications. However, with an average lifespan of 3 to 5 years,[1] the disposal of these batteries is a growing concern. It is estimated that global LIB waste may exceed 460 000 tons by 2025,[2] with projections that it will reach nearly 1.2 million tons by 2030.[3] Therefore, LIB recycling has primarily concentrated on recovering essential metal components such as lithium, copper, aluminum, manganese, and nickel, or recycling them into other valuable materials.[4–8] Otherwise, converting metals into valuable products is another strategy to solve serious environmental problems and relieve the scarcity of metals.[9–11] In another strategy, the direct regeneration of electrode materials is attempted.[12–15] There are many works reported on recycling spent graphite or the modification of spent graphite materials for a second life in LIBs.[16] Moreover, researchers have also attempted to find suitable methods to recycle all the components of spent LIBs.[17–19] However, direct regeneration faces many challenges, such as impurity contamination, material deterioration, intricate separation processes, and difficulties in fully restoring the original performance. Therefore, upcycling can offer an alternative approach to repurposing spent electrode materials into high-value applications through efficient and sustainable strategies such as Li–S batteries,[20] dual carbon batteries,[21] electrocatalysis,[22] *etc.*

Department of Chemistry, Indian Institute of Technology Hyderabad, Kandi, Sangareddy, Telangana, 502284, India. E-mail: martha@chy.iith.ac.in

Meanwhile, with the heightened demand for energy-power-balanced renewable energy systems, the research has focused on lithium-ion capacitors (LICs) technology combining high energy density, fast charge/discharge rates, and long cycle life.[23–27] A typical LIC consists of a LIB battery-type anode, which can be categorized into intercalation, conversion, and alloy type.[28–30] In contrast, the cathode is often made of high surface area activated carbon, which stores charges through the adsorption–desorption of ions on its surface. This non-faradaic charge-storage process in the cathode is pivotal for achieving rapid power delivery for LICs.[31–33] However, the different charge storage mechanisms in cathode and anode materials create a kinetic and capacitive mismatch and limit the broader commercial adoption of LICs. Several strategies for the anode, such as controlling the electrode morphology,[34,35] introducing carbon coating,[36,37] and doping with other elements,[38–42] have been developed in the literature to overcome the challenges by improving conductivity and cycling stability. In contrast, a high specific surface area with an appropriate pore-size distribution[43,44] and the introduction of beneficial functional groups[45,46] were investigated for the cathode part.

The present study investigates the development of an LIC device utilizing the spent LIB components, focusing on material upcycling and optimizing performance, as follows: (1) integrating both recovered materials into a carbon fiber mat-supported LIC device demonstrates a sustainable, binder-free, and flexible architecture, which has not been reported in our prior work. (2) Direct calcination of the LCO + graphite black mass (without prior separation) under optimized conditions to generate a mixed cobalt oxide (mCO-R) phase with improved structural features and electrochemical properties suitable for anode application. (3) Tailored KOH activation and thermal treatment of the recovered graphite to obtain activated graphene oxide (AGO-R) with significantly controlled porosity compared to previous protocols.

Herein, the graphite anode of spent LIBs is transformed into activated graphene oxide (AGO-R) to act as a cathode for the LICs. The generated AGO-R can have the following advantages: (i) excellent electrical conductivity due to the restoration of sp^2 carbon domains, (ii) provides abundant active sites for ion adsorption, (iii) reduces the dependency on pristine graphene and minimizes waste. This environmentally friendly and cost-effective approach makes it suitable for sustainable energy storage applications. On the other hand, the $LiCoO_2$ cathode of spent LIBs is converted into a mixed cobalt oxide and acts as an anode for LICs. Utilizing recycled LCO reduces waste and promotes the circular economy by reusing cobalt, a critical and expensive raw material. Mixed cobalt oxides typically exhibit high lithium storage capacity and enhanced pseudocapacitive properties. Mixed cobalt oxide can exhibit porous structures that allow efficient ion transport and good electrical conductivity, strengthening the power capability of LICs.

Furthermore, the cathode and anode materials are coated on a carbon fiber mat, which mainly acts as a current collector and contributes some capacity. This architecture shows a uniform distribution of active materials, accommodates volume changes, and allows efficient electrolyte percolation in the internal void space, resulting in good rate capability and cycle life. Moreover, it is more environmentally friendly compared to metals like copper and aluminum. Thus, this configuration fulfills the design of sustainable, flexible, and energy-power-balanced LIC devices.

2 Experimental details

2.1 Extraction of black mass from spent LIBs

The black mass containing LCO-type cathode and graphite anode mixture recovered from spent LIBs. 18 650-type cylindrical cells from discarded battery packs are discharged below 2.0 V in the brine solution. The cells were dismantled. The black mass was recovered by a mechanical separation process that involves crushing and multiple stages of sieving based on different mass fractions and density separation techniques.

2.2 Synthesis of cobalt oxide (mCO-R)

The black mass mixtures of LCO and graphite material were subjected to direct calcination at 850 °C for 12 hours in an air atmosphere. Spent LCO-type cathodes primarily consist of a lithium-deficient $LiCoO_2$ phase and a converted spinel Co_3O_4 phase. During the high-temperature calcination process, the carbon from the anode aids in the carbothermal reduction of $LiCoO_2$, producing Co_3O_4 as the main product and CoO, metallic cobalt, and Li_2CO_3 as byproducts. This process likely results in Co_3O_4 as the predominant product and CoO, metallic Co, and Li_2CO_3 as secondary products.

2.3 Spent graphite to activated graphene oxide (AGO-R)

Graphite was mechanically separated from the copper current collector. The separated graphite was washed with water and calcined at 750 °C under an inert atmosphere to remove all organic impurities (hereafter, the calcined graphite is termed recovered graphite, RG). One portion of this RG was then converted to graphene oxide (GO-R) through a modified Hummers' method.

For AGO-R synthesis, GO-R was impregnated with KOH in a 1 : 6 ratio at 130 °C for 24 h. The dried mass was then calcined in an inert atmosphere at 800 °C to impart efficient porosity.

2.4 Physical characterization

The structure and phase are characterized by using a powder X-ray diffractometer (Empyrean, Panalytical) with Cu Kα (1.54 Å) as a radiation source, operated at a voltage of 40 kV and current of 30 mA, in the 2θ angle range of 10° to 70°. The surface morphology of the materials is recognized by scanning electron microscopy SEM (FESEM, JEOL-JEM 2011 instrument, Japan). X-ray photoelectron spectroscopy (XPS) (Axis Supra Kratos Analytical Pvt. Ltd) analyzes the surface functional groups or oxidation states of the constituent elements. The XPS data are deconvoluted into Gaussian functions after calibrating the data concerning the main C 1s peak at 284.6 eV. The fitting and analysis are done using OriginPro 9.0 software. A N_2 adsorption–desorption study is followed to estimate the BET surface area and pore size distribution of the composite material.

Attenuated total reflection-infrared (ATR-IR) spectra are recorded from a Bruker Tensor 37 spectrophotometer.

2.5 Electrode preparation and cell assembly

The electrode preparation procedure typically involves several steps, such as slurry mixing, coating, calendaring, and drying. At first, the desired number of active materials, conductive additives (Super P C65, TIMCAL Ltd, Switzerland), and PVDF binder (Kureha, KF polymer # 1700) in 80 : 10 : 10 ratios are weighed accurately. They are mixed and dispersed thoroughly in NMP solvent (Sigma-Aldrich) to make a homogeneous and consistent viscous slurry. Then, active materials are coated on current collectors (carbon fiber), which are dried at 80 °C overnight in a vacuum oven, followed by hot calendaring and punching into 10 mm circular discs. The loading of the active mass is maintained at ~2.2 ± 0.3 mg cm^{-2}.

2.6 Electrochemical characterization

The electrochemical characterization of cathode and anode half-cells was conducted using a two-electrode system, with lithium metal serving as both the reference and counter electrode. CR2032 coin-type cells were assembled in an argon-filled glove box (MBraun, Germany), where oxygen and moisture levels were maintained below 0.1 ppm. During assembly, a PP/PE/PP trilayer separator pre-soaked in 1 M $LiPF_6$ dissolved in EC : DEC (1 : 1) electrolyte was placed between the electrodes. Galvanostatic charge–discharge (GCD) measurements, including cycling and rate capability tests, were performed using Biologic instruments BCS 805 system (France). The GCD cycling and C-rate performances are carried out in the voltage range of 0.01 to 3 V for the mCO electrode and 1.5 to 4.0 V for the AGO-R cathode. C-rate study involves different current densities of 0.05, 0.1, 0.2, 0.5, 1, 2, and 5 A g^{-1}. Cyclic voltammetry (CV) and Electrochemical Impedance Spectroscopy (EIS) are studied in the Solartron (Oak Ridge, USA) 1470E multichannel potentiostat system coupled with a 1455A frequency response analyzer. During EIS measurement, the frequency range is maintained between 1 MHz and 10 mHz with a voltage perturbation of 10 mV.

3 Results and data analysis

3.1 Physicochemical and morphological characteristics

3.1.1 Activated graphene oxide – partially in-plane ordered amorphous, defective structure with balanced micro-meso porosity and fragmented graphene sheets. The Phase and structural characterizations of AGO-R are carried out and shown in Fig. 1. The XRD pattern (Fig. 1a) shows two broad peaks at 2θ = 22.23 and 43.83°, indicating the amorphous nature of the AGO-R materials. A comparatively more intense peak than other

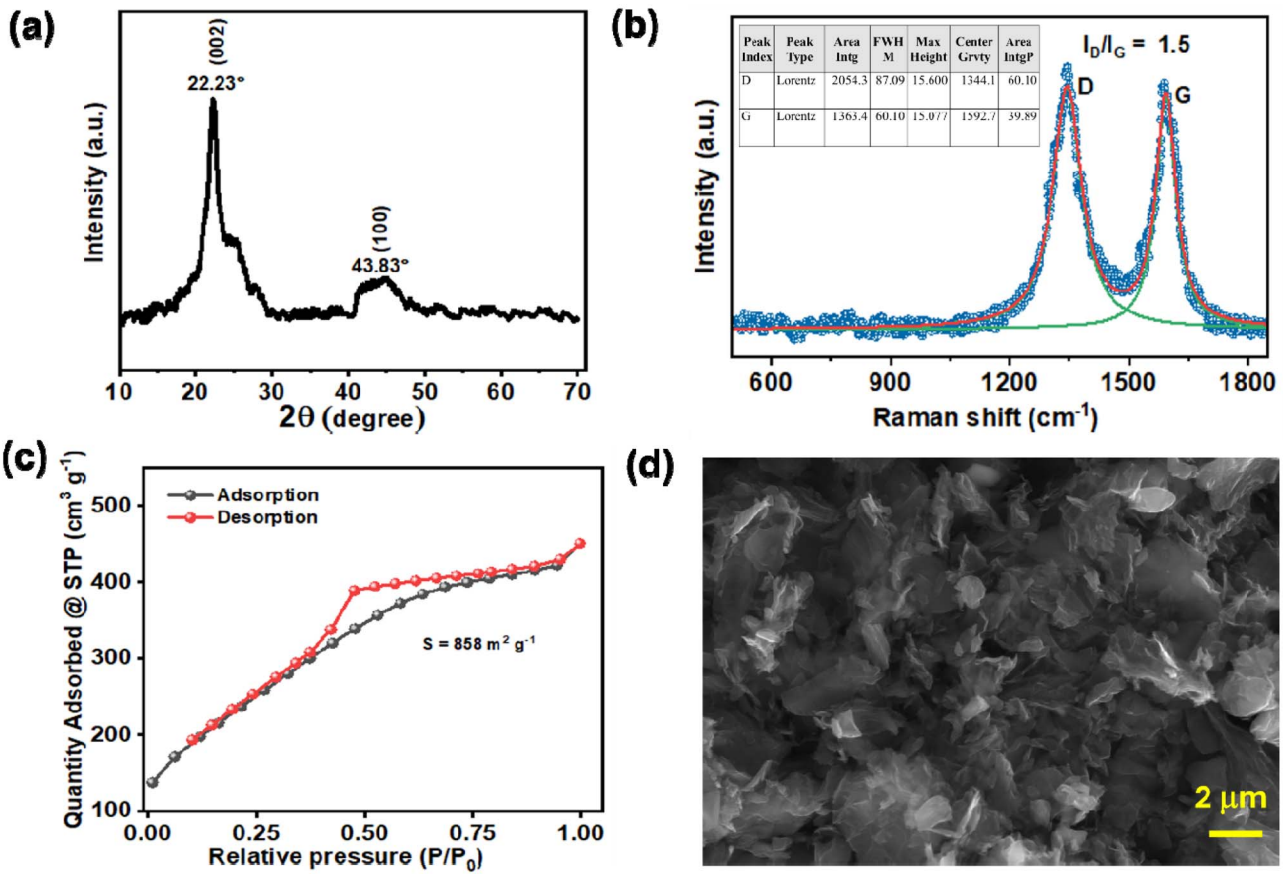

Fig. 1 (a) XRD diffractometer, (b) Raman spectra, (c) N_2-adsorption–desorption isotherm, (d) SEM images of AGO-R materials.

activated carbon at $2\theta = 43.83°$ suggests an in-plane nature, signifying an improved electronic conductivity of the present activated carbon (AGO-R). The amorphous and conductive nature of AGO-R materials is beneficial for high-rate cathodes for LICs.

The presence of the D and G bands in Raman spectra (Fig. 1b) indicates the sp^3-bonded carbon atoms. The calculated I_D/I_G value is 1.5 (considering the integral area under the peak), suggesting a slightly greater degree of disorderness. The higher disorderness in the carbon structure aids in more adsorption capacity. The N_2 adsorption–desorption study (Fig. 1c) revealed the presence of surface area and pore structure in the materials. The estimated surface area is 857 $m^2\ g^{-1}$, corresponding to the type I and IV isotherm according to the IUPAC nomenclature. The pore size distribution is plotted in Fig. S1, showing that the average pore size is 3.1 nm, with ample amount distribution in the microporous region, indicating the mixture of meso and micropores. This combined feature can facilitate ample accommodations and smooth transportation of more ions. The SEM image exposes the surface morphology of AGO-R. The SEM image (Fig. 1d) reveals a porous and fragmented graphene nanosheet structure. This indicates the activation process that leads to forming a structure conducive to improved ion adsorption. Furthermore, the TEM images (SI Fig. S2a) reveal irregularly shaped carbon particles with disordered domains. High-resolution TEM (HRTEM) images (Fig. S2b) display short-range graphitic layers, turbostratically arranged, indicating partial ordering with a lack of long-range crystallinity. These structural characteristics are typical of activated carbon and are beneficial for improved ion transport and surface accessibility for EDLC-type charge storage phenomena during the function of LICs.

3.1.2 Mixed cobalt oxide composites – Co_3O_4 and CoO as key active materials, and metallic Co improves electronic conductivity. On the other hand, the required physical characterizations of the mCO-R are studied and shown in the SI file. The detailed characterizations of mCO-R have already been discussed in our previous communications.[47] The XRD pattern (Fig. S3a) confirms the presence of primarily mixed cobalt oxide, such as Co_3O_4 and CoO, which are the key active materials. The presence of metallic cobalt confers better electronic conductivity to the composites. The XPS survey spectrum of the mCO-R electrode (Fig. S3b) shows peaks corresponding to Co, O, and C, along with an F 1s signal (~682 eV) originating from PVDF binder used during electrode preparation. The Co 2p region confirms the presence of cobalt oxides, while the O 1s and C 1s peaks indicate lattice oxygen and adventitious carbon. The deconvoluted XPS study (Fig. S3c and d) reveals the presence of Co^{2+} and Co^{3+} states of the cobalt, further confirming the existence of both cobalt oxides (Co_3O_4 and CoO) phases. The SEM (Fig. S4a and b) shows an ordered stacking-type surface morphology of the mCO-R particles. Fig. S4c displays the CF current collector's morphology, showing the fiber strands and void spaces to accommodate volume expansion and electrolyte infiltration.

Furthermore, TEM analysis assesses the upcycled composite metal oxide's particle morphology and microstructural features. The low-magnification images (Fig. 2a) demonstrate nanosized particles with relatively uniform size distribution. TEM micrograph of one particle (Fig. 2b) shows fine particles with an average size of ~200–300 nm. High-resolution TEM (HRTEM) images (Fig. 2c) clearly show lattice fringes with different types of interplanar spacing corresponding to different other planes and components present in the composite, indicating the crystalline nature of the material. Moreover, the d-spacing of

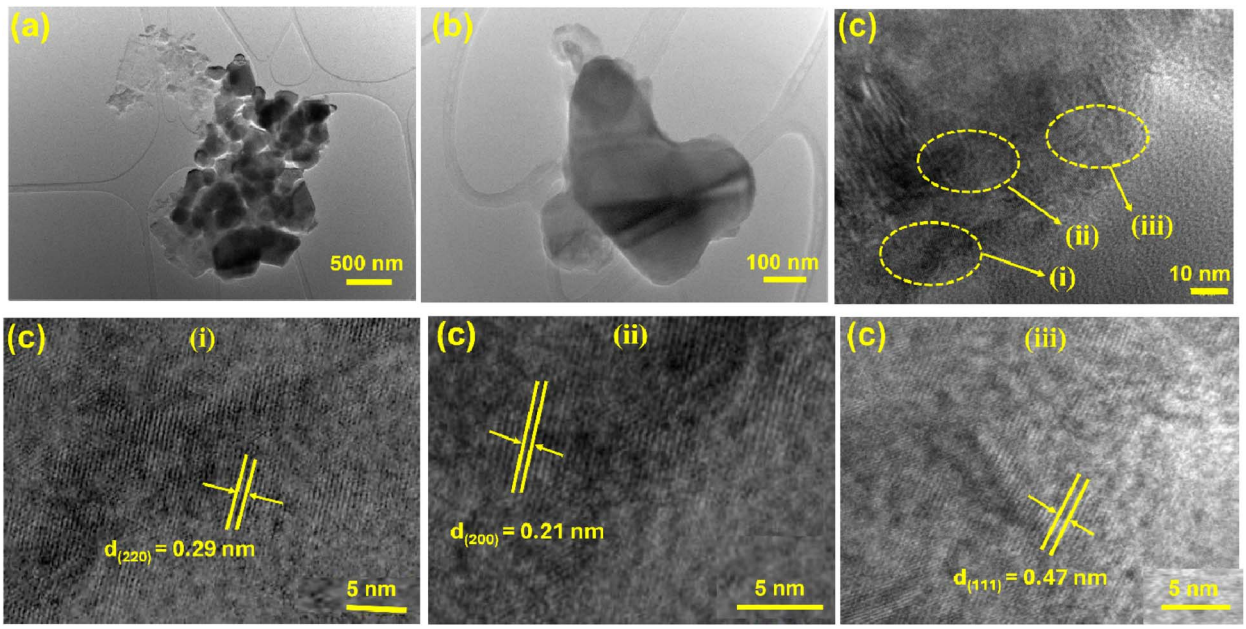

Fig. 2 (a) Low magnification TEM image, (b)TEM micrograph of a single particle, (c) different lattice fringes, (c-i) $d = 0.29$ nm corresponding to (220) of Co_3O_4, (c-ii) $d = 0.21$ nm corresponding to (200) plane of CoO, and (c-iii) $d = 0.47$ nm (111) plane of Co_3O_4 crystal, of mCO-R materials.

distinct lattice fringes from different regions marked by (i), (ii), and (iii) in Fig. 2c are shown separately to understand the lattice fringes and their corresponding d-spacing values precisely. The d-spacing of 0.29 nm (Fig. 2c-i) and 0.47 nm (Fig. 2c-iii) corresponds to the (220) plane and (111) plane of the Co_3O_4 crystal, respectively. On the other hand, the d-spacing value of 0.21 nm corresponds to the (200) plane of the CoO crystal structure, present in the composite.

Thus, all the above physical and morphological characteristics suggest the formation of electrochemically active nanostructured mixed cobalt oxide. These physicochemical characteristics can be favorable for the high-rate anode for LICs, as discussed in the electrochemical performance sections.

3.2 Electrochemical performances

3.2.1 Cathode half-cells analysis (*vs.* Li^+/Li)

3.2.1.1 EDLC behavior, negligible IR drop, high rate capability – showcasing better material conductivity and electrolyte infiltration through the CF current collector. The CV and GCD of CF-AGO-R are consistent with the EDLC type of behavior, as expected. The CVs (Fig. 3a) show quasi-rectangular plots at various scan rates in the voltage range from 1.5 to 4 V, indicating a reversible adsorption–desorption ion storage phenomenon at the surface of the electrode.

At the same time, the triangular linear form of the charge–discharge graph (Fig. 3b) confirms the EDLC mechanism, primarily governed by the adsorption and desorption of ions. Again, the negligible IR various current densities at low to higher rates suggest excellent electronic conductivity as evidenced by the in-plane ordered and a lesser degree of disorderness the XRD and Raman of the AGO-R materials. Besides, using a CF current collector is vital in reflecting better electronic and ionic conductivity through its 3D network. The specific capacity is calculated at various current densities, tabulated in Table S1. It is seen that CF-AGO-R can deliver a maximum capacitance of ~150 F g^{-1} at a medium current density of 0.3 A g^{-1} and ~90 F g^{-1} at a higher current density of 2 A g^{-1}. The good retention in capacity after 5000 repeated charge–discharge cycles (Fig. 3c) indicates the robust structural integrity of the material provided by the well mechanical strength and electrolyte infiltration of the CF current collector. Moreover, the consistently high coulombic efficiency throughout the cycling indicates minimal side reactions, good structural stability, and high reversibility of the electrochemical reactions. All the combined electrochemical performances accentuate the material's potential for operating as a cathode in LICs. Fig. 3d shows the Nyquist plots of the CF-AGO-R cathode half-cell before and after cycling. The plot shows significant

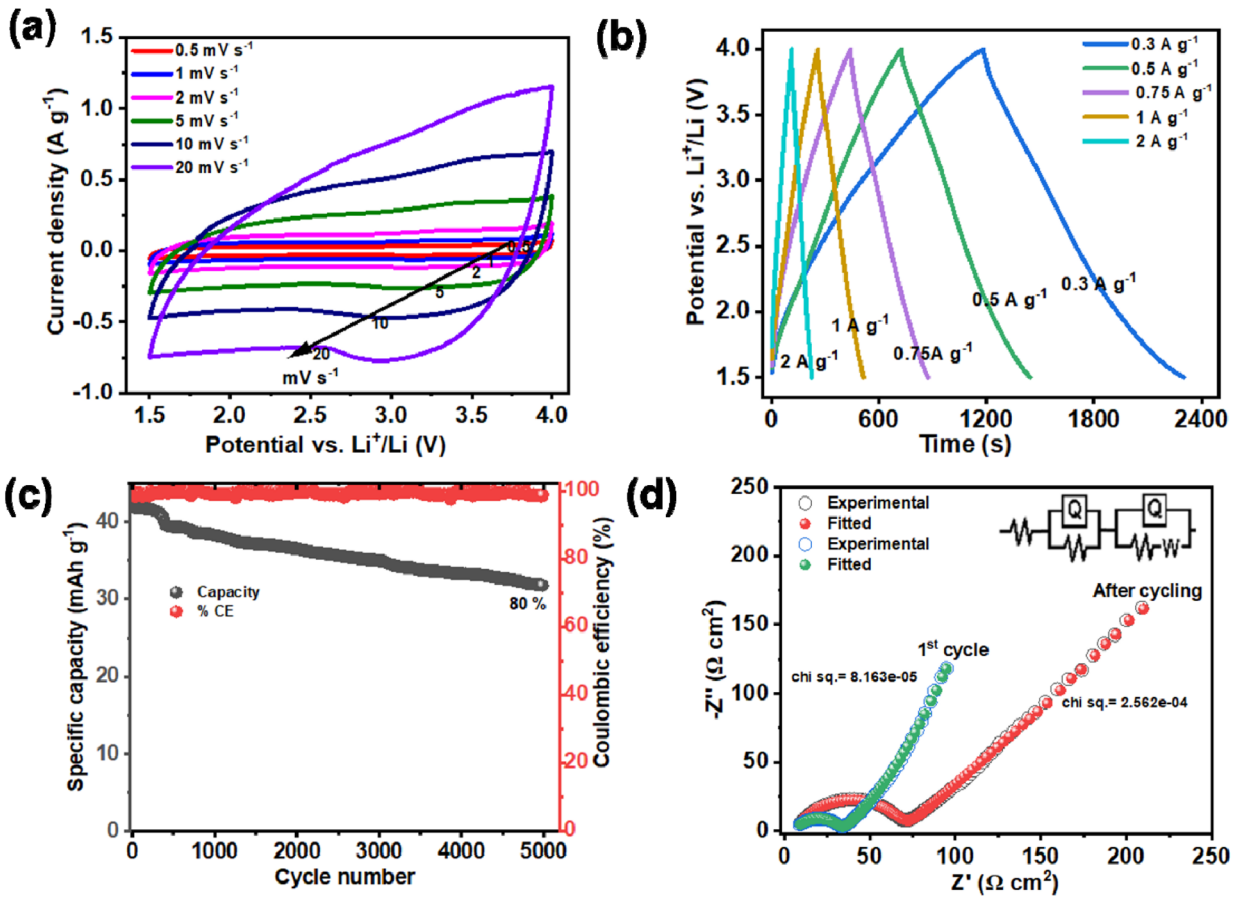

Fig. 3 (a) Cyclic voltammogram, (b) voltage profile, (c) cycling stability, (d) EIS spectra and equivalent circuit model (inset) for the CF-AGO-R cathode half-cell *vs.* Li^+/Li.

changes only in the R_{ct} value, indicating the enhanced interfacial resistance due to the reduced active surface area and pore-blocking caused by the degradation products on the surface.

3.2.2 Anode half-cell analysis (*vs.* Li^+/Li)

3.2.2.1 Better reversibility, high-rate capability, and cycling stability – suggestive of better material conductivity and utilization of void spaces of CF to buffer the volume expansion. The cyclic voltammogram at 0.05 mV s^{-1} (in Fig. 4a) and galvanostatic charge–discharge at 30 mA g^{-1} (Fig. 4b) of the CF-mCO-R have been studied in the voltage range of 0.01 to 2.5 V to understand the Li-ion storage behavior of mCo-R at a high rate for the application as anode in LICs. Fig. 4a depicts a prominent, broad cathodic peak around 1 V during the initial lithiation process, which corresponds to the electrochemical reduction of Co_3O_4 and CoO to Co^0 within an amorphous Li_2O matrix, accompanied by the formation of a solid electrolyte interface (SEI) on the electrode surface. In the subsequent cycles, this reaction occurs at two distinct redox potentials, 1.03 and 1.24 V, indicating multistep electrochemical reactions occurred between Li^+ and Co_3O_4/CoO.

The corresponding anodic peak occurs in one step at 2.02 V, which can be attributed to the reaction between Co and Li_2O with the concomitant decomposition of Li_2O. The cathodic and anodic peak intensity decreases in the subsequent cycle, ascribed to the newly formed amorphous nature of Li_2O, Co products, and the reproduced CoO and Co_3O_4 phases. The other reduction peaks at 0.17 and 0.01 V can be ascribed to the intercalation of Li^+ ions into the carbon residue in the mCO-R sample and in the carbon fiber matrix of the current collector.

The stable GCD profile (Fig. 4b) (second cycle onwards) shows a long plateau and short plateau, starting from 1.23 V and 0.12 V, respectively, corresponding to the two-step reactions associated with the reaction between lithium and cobalt oxides, supporting the CV plots of Fig. 3a. The deliverable capacity in the first cycle is 870 mAh g^{-1}, which is reduced to 698 mAh g^{-1} in the second cycle. The loss (<20%) is obvious due to the formation of the solid electrolyte interphase caused by the reductive decomposition of the electrolytic solvent in the first cycle. However, the loss is minimal compared to the reported work, which can be explained by residual Li-salts in the mCO-R sample, which minimizes the Li-ions consumption during 1st cycle.

The rate capability study of mCO-R (Fig. 4c) has been carried out to understand the high-rate capability of the materials required to use it as an anode for LICs. The CF-mCO-R electrode shows a reasonable capacity of 325, 262, and 155 mAh g^{-1} at a higher current density of 0.5, 1, and 2 A g^{-1}, respectively. The results show good compatibility with EDLC-type cathode materials, showing a maximum capacity of 80–100 mAh g^{-1}. This high-rate capability of the composite electrode is feasible due to the excellent conductivity arising from the synergistic effect of the CF-based current collector and pre-existing metallic

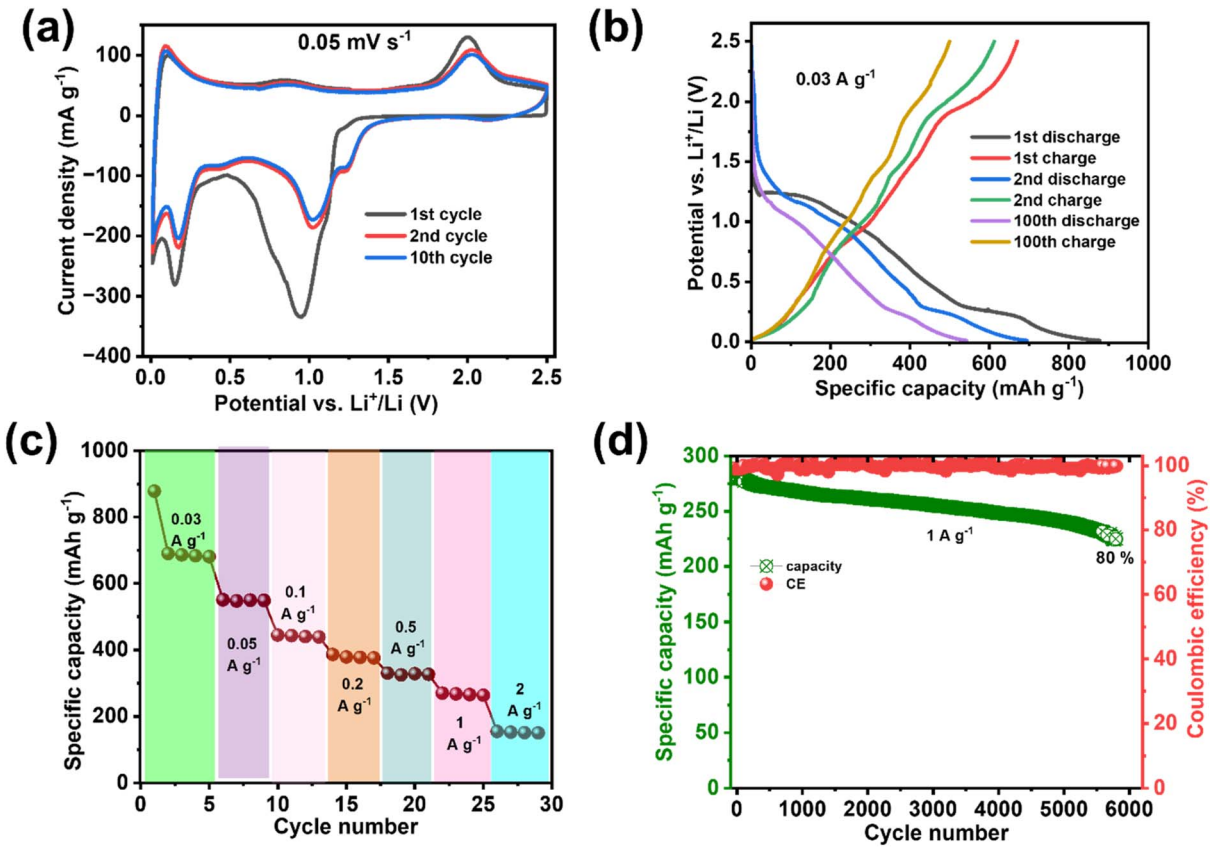

Fig. 4 (a) Cyclic voltammogram at 0.05 mV s^{-1}, (b) GCD profile at 0.03 A g^{-1}, (c) C-rate studies at various current densities of 0.03, 0.05, 0.1, 0.2, 0.5, 1, and 2 A g^{-1}, (d) cycling stability plot with coulombic efficiency at 1 A g^{-1}, of in the voltage range of 0.01 to 2.5 V for CF-mCO-R half-cell.

Co in the active materials. Moreover, the utilization of the CF matrix provides smooth electrolyte percolation and structural integrity for the active materials even at higher currents.

The high rate cycling stability of the CF-mCO-R half-cell is studied at 1 A g^{-1} (Fig. 4d). It shows 225 mAh g^{-1} capacity starting from 280 mAh g^{-1}, rendering ~80% capacity after 6000 cycles. The rationally good cycling stability at a high rate is possible because of the 3D framework of the carbon fiber-based current collector, which plays a crucial role in housing the volume expansion that occurs by the repeated conversion reaction with cycling.

Furthermore, the CV plots (Fig. 5a) are conducted at different scanning rates of 0.1, 0.2, 0.5, 1, and 2 mV s^{-1} to elucidate the charge storage kinetics and evaluate the capacitive and diffusive contributions.

It is observed that the redox peaks become broader with the increase in the scan rates. Using the power law, the *b*-value is calculated at a particular redox potential. The *b*-value is close to 0.5 at the lithiation–delithiation potential of cobalt oxide, *i.e.*, cathodic 0.7 V and anodic 2 V, as shown in Fig. 5b and c, respectively. The *b* value indicates that the charge-storage process is mostly diffusion-limited during the conversion reaction of cobalt oxide with lithium. Moreover, the charge storage kinetics in other potentials are also determined and shown in Fig. S5. The resulting *b*-values (~0.67) suggest that the charge storage processes that occurred at 0.12 and 0.86 V are a combination of both capacitive and diffusive control.

Using the Trasatti method, the diffusive and capacitive percentages are separated, as shown in Fig. 5d and e. It was found that the capacitive percentage increased from 17 to 49% with the increase in the scan rate from 0.1 to 2 mV s^{-1} during the lithiation reaction into cobalt oxide. On the other hand, the capacitive contribution increases from 30 to 66% during the delithiation in response to cobalt oxide. Fig. 5f exhibits the capacitive percentage of the total charge storage process through CV at 0.2 mV s^{-1}. The capacitive contribution of 38%, even at a medium scan rate of 0.2 mV s^{-1}, implies the good rate capability of the materials, which is beneficial as an anode for the full cell LICs.

3.2.3 Full-cell analysis: hybrid LIC (CF-mCO-R//CF-AGO-R) devices

3.2.3.1 Optimum mass ratio and voltage range – for energy-power balance and good cycle life. Lithium-ion capacitors (LICs) were developed using CF-AGO-R as the positive electrode material and prelithiated CF-mCO-R as the negative electrode material. The optimum mass ratios for the full LIC cell are optimized by making and testing the cells at different mass ratios. The rate capability study in Fig. S6 shows the obtained capacity at lower (0.2 A g^{-1}) to higher current densities (5 A g^{-1}) for the different anode-to-cathode mass ratios. It is observed that the deliverable capacity is stable and greater for 1 : 2 than for the other mass ratios across all the current densities. The corresponding LICs provide 47 mAh g^{-1} capacity at 0.1 A g^{-1} and 25 mAh g^{-1} at a higher current of 5 A g^{-1}. Further, the optimum voltage range is determined by studying the reflection in cycling stability at different voltage ranges of 1 to 4, 1 to 3.6 V, and 0.5 to 3.6 V (Fig. S7). It is noted that the decay in capacity is very fast, although the initial capacity is higher. Again, the maximum available capacity is reduced by lowering the cut-off voltage. Hence, the optimum voltage range is 1 to 3.6 V.

3.2.3.2 Full-cell – storage mechanisms, a reflection of battery-type materials, lead to improved energy density, retaining

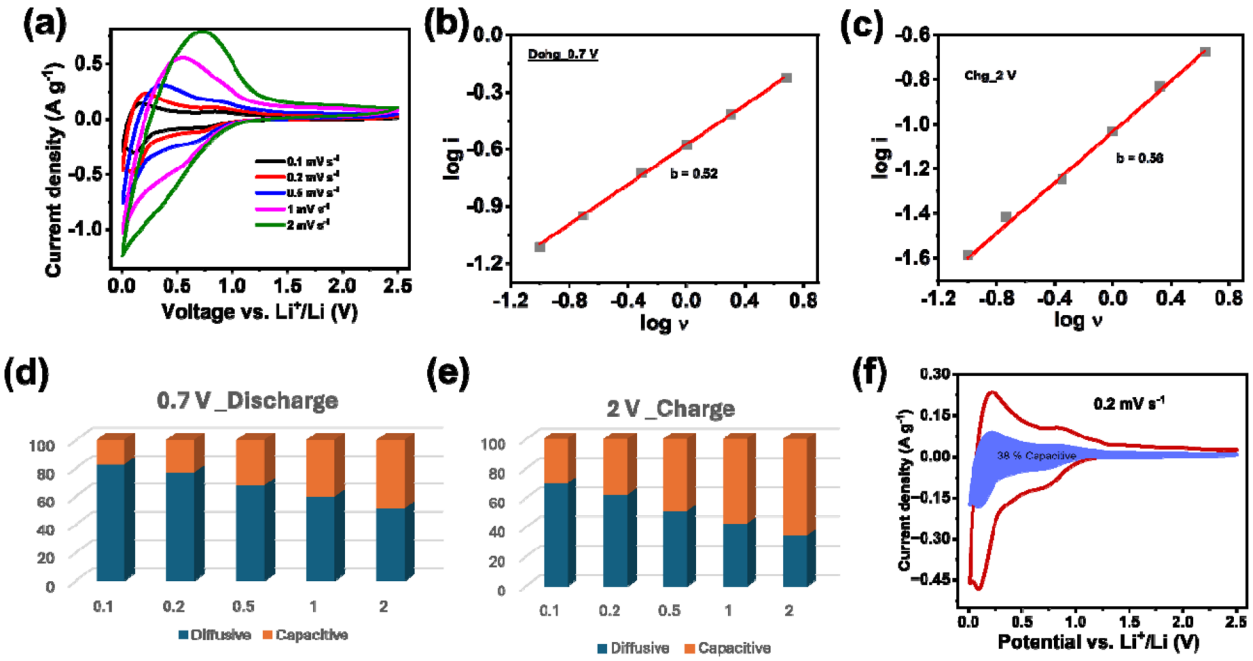

Fig. 5 (a) CV at various scan rates of 0.1, 0.2, 0.5, 1, and 2 mV s^{-1}; log '*i*' *vs.* log '*ν*' plot (b) at cathodic peak 0.7 V, (c) at anodic peak 2 V; (d) capacitive and diffusive percentage at various scan rates corresponding to (d) 0.7 V peak, (e) 2 V peak; (f) the capacitive contribution to the total charge storage at 0.2 mV s^{-1}, for CF-mCO-R half-cell.

a significant cycle life of EDLC. The mechanism of the charge storage phenomenon involved in the LICs is explained in Fig. 6a. During charging, the migration of PF_6^- ions into the layered porous structure of the AGO-R and CF current collector of the positive electrode, while Li^+ ions are intercalated or adsorbed onto the surface of the mCO-R and CF structure in the negative electrode. The reverse phenomena of these steps occur during the discharge process.

The CV curves of optimized LIC (the anode/cathode mass ratio of 1 : 2 and 1 to 3.6 V) are presented in Fig. 6b. The curves are almost quasi-rectangular at the scan rates range from 0.2 to 10 mV s^{-1}, with the presence of a redox hump after 2.6 V, confirming the hybridization of EDLC-type cathode with LIB-type anode. This suggests a redox reaction accompanied by the conversion and intercalation of Li-ions with the CF-mCO-R electrode. To gain further insights, galvanostatic charge–discharge experiments were performed at different current densities, as shown in Fig. 6c and d. The profile deviates from the linear triangular plot, revealing the involvement of two distinct charge storage mechanisms in the LIC. However, a reduction in discharge time is observed as the applied current rate increases, which is an expected behavior. Again, the

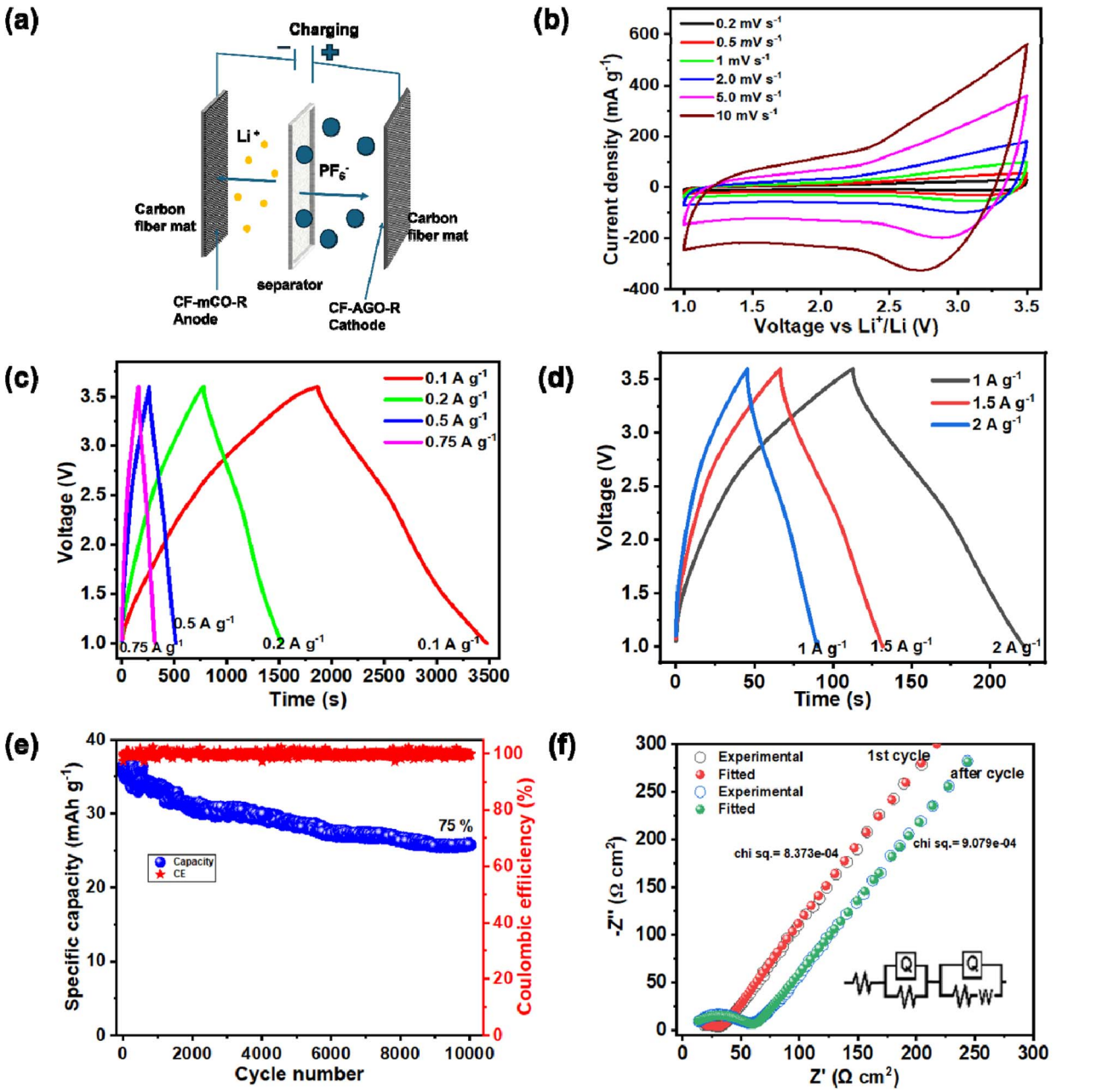

Fig. 6 (a) The charge storage mechanism in full cell LIC during charging, (b) cyclic voltammogram at different scanning rates of 0.2, 0.5, 1, 2, 5, 10 mV s^{-1}; charge–discharge profile (c) at the medium current rate of 0.1, 0.2, 0.5, 0.75 A g^{-1} (d) at the higher current rate of 1, 1.5, 2 A g^{-1} (e) cycling stability plot at 1 A g^{-1} and (f) fitted EIS plot and corresponding equivalent circuit model (inset) before and after cycling, for CF-mCO-R//CF-AGO-R LIC device.

charge–discharge plot at higher current rates results in a shorter discharge time, reflecting the limited utilization of the active materials in the faradaic reactions. A critical aspect of the hybrid system's performance is the cycling stability, which is shown in Fig. 6e. The optimized LIC can run at 1 A g^{-1} current density for 10 000 cycles, showing 75% retention with an average coulombic efficiency of 99.48%. This confirms the long-term stability of the LIC device constructed by the CF-mCO-R anode and CF-AGO-R cathode.

To understand the nature of the interfacial and diffusion behavior of the electrode with cycling, the EIS has been studied and presented as a Nyquist plot in Fig. 6f. The impedance corresponding to the high-frequency region refers to solution resistance (R_s). An increase in the R_s value from R_s. The negligible change in R_s value after 10 000 cycles supports the materials' good electronic and ionic conductivity and CF backbone. However, the capacity fading can be correlated with the increase in the R_{ct} value and the Warburg tails. The significant rise in R_{ct} value from 26.6 to 57.5 Ω is due to the growth of the interfacial charge-transfer resistance across the electrode and electrolyte interphase, resulting from the parasitic reactions with long-term cycling. Moreover, a reduction in the slope of the low-frequency Warburg tails suggests pore blockage and interference with capacitive charge storage. These factors collectively lead to the performance degradation of the LIC cell after 10 000 cycles.

Furthermore, post-mortem SEM analysis was performed on the electrodes after 10 000 cycles to assess their structural stability; the comparison images are shown in Fig. S8. Both mCO-R and AGO-R maintained their overall morphology without noticeable pulverization or delamination, indicating excellent mechanical robustness. Only minor surface roughening was observed, likely due to prolonged electrolyte interactions. Notably, mCO-R exhibited smaller and more uniform particle sizes than its pristine state, suggesting gradual particle refinement during cycling. This may have contributed to its sustained electrochemical performance over extended operation. These observations confirm the mechanical and structural robustness of the electrode materials.

3.2.3.3 Practical viability of the full-cell LIC device – negligible leakage current and improved self-discharge rate. The practical applicability of the LIC device is comprehensively evaluated by the Ragone plot (Fig. 7a), which describes the comparative value of energy and power density. The capacitance and energy-power value of the full cell are calculated at different current densities and shown in Table S2. This LIC device exhibits a higher energy

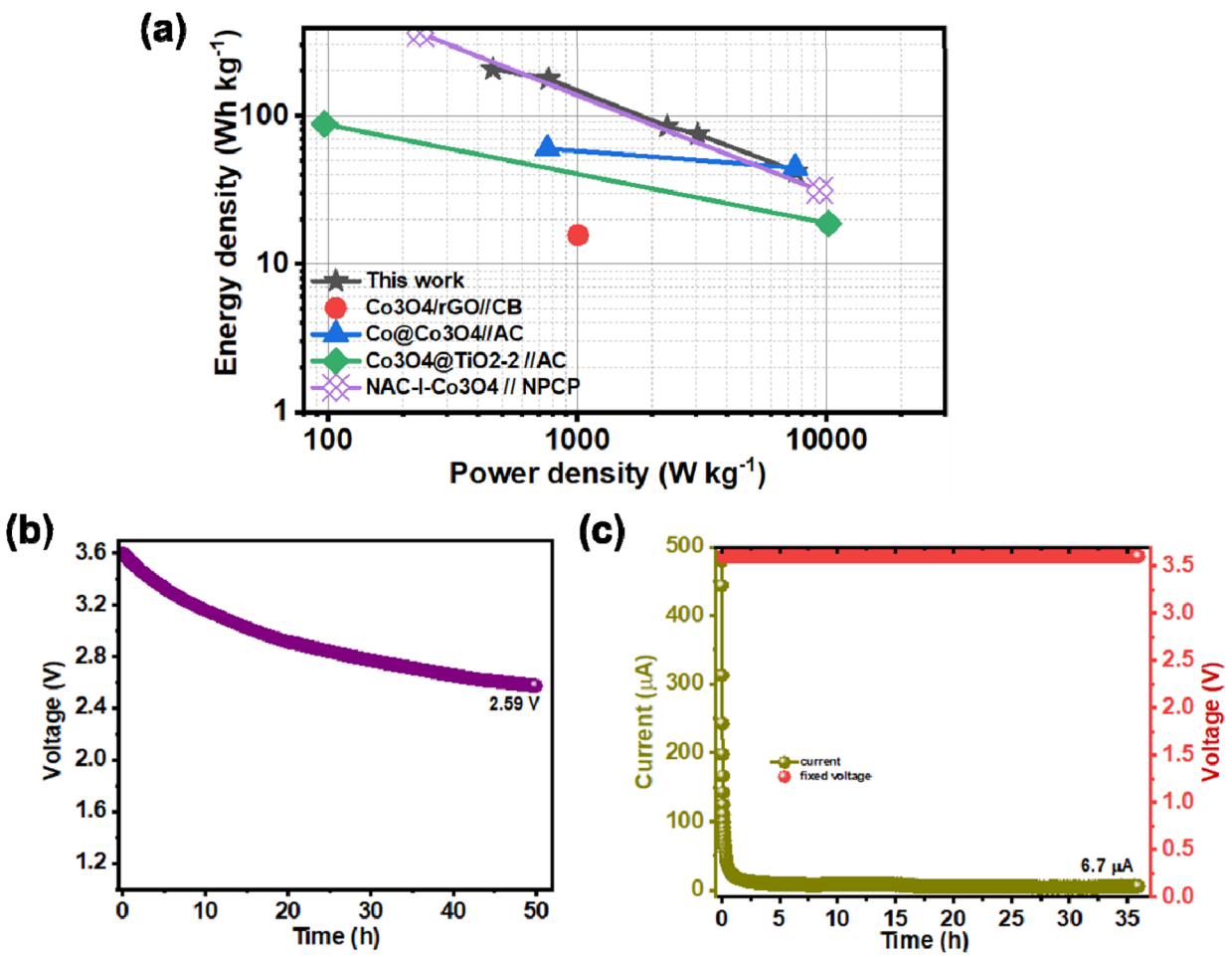

Fig. 7 (a) Ragone plot of the full cell device, comparing with some literature work, (b) self-discharge study, (c) leakage current study for the CF-mCO-R//CF-AGO-R LIC device.

density of 42 Wh kg^{-1} at a power density of 7560 W kg^{-1}, indicating improved electrochemical performance. However, the value is compared with the literature value in Table S3, showcasing the superior results of the present work in terms of energy-power balancing with satisfactory cycle life.

This enhancement is attributed to the synergistic combination of the EDLC-type positive electrode and pre-lithiated battery-type negative electrode and the use of a 3D carbon framework as the current collector, which facilitates efficient charge storage mechanisms even at high rates.

Another important practicality parameter of LICs is self-discharge, particularly for applications requiring extended standby periods. Herein, the self-discharge behavior of the LIC was monitored by recording the open-circuit voltage over 50 hours (Fig. 7b). The device retained approximately 72% (2.59 V) of its initial voltage (3.6 V) after 50 hours, indicating low self-discharge rates compared to other reported LIC systems. The observed low self-discharge is primarily attributed to the stable electrochemical behavior of the LICs. This ensures minimal energy loss during idle periods and improves energy efficiency.

Further, Leakage current is studied to reflect the device's self-discharge behavior. The leakage current of the LIC was measured by applying a constant voltage of 3.6 V for 35 hours (Fig. 7c). The steady-state current flow is recorded to be 6.9 μA, which has stabilized for 3 hours, indicating minimal parasitic reactions and excellent electrochemical stability.

4 Discussions

This study utilizes the spent LIB's electrodes to upcycle them to the LIC's electrode. This involves the transformation of the recovered electrode from spent LIBs into valuable materials, followed by the conjunction of a 3D carbon fiber current collector to make the electrode. The approach has proven to be effective in addressing the challenge of achieving a balance between energy density and power density in LICs.

The improved energy density of the LIC is attributed to the porous structure of the CF-AGO-R, which facilitates ion adsorption and charge storage. The pre-lithiated CF-mCO-R electrode enhances the faradaic contribution, improving the overall charge storage capacity. In addition, 3D carbon fiber, a freestanding electrode, facilitates the high rate capability due to its smooth and faster ionic movement through the 3D framework and electrolyte percolation.

While the LICs demonstrated promising performance, future studies could focus on developing scalable synthesis methods and investigating advanced electrolytes to reduce self-discharge rates.

Additionally, a comparative table (Table S4) summarizes key parameters from the cited works—such as source of recycled materials, processing methods, device configurations, and performance metrics—and contrasts them with the current study. Compared to previous reports that regenerate specific cathode or anode components through multi-step recovery and synthesis, our approach directly reuses the mixed black mass from spent LIBs with minimal processing. This simplifies the recycling route and enables simultaneous integration of both active components into a carbon fiber-supported LIC device. Such a strategy significantly reduces chemical usage, energy input, and processing time, offering a more sustainable and scalable pathway for high-performance energy storage systems.

5 Conclusions

In summary, the electrode materials from the end-of-life spent LIBs are successfully recovered and upcycled into the electrode for high-rate capable LICs. The free-standing film is made for LIC electrodes by using a carbon fiber-based current collector. The void spaces in the 3D unique woven networks can accommodate volume expansion for conversion-type cobalt oxide anode material acting as a protective buffer and active sites and conductive filler, thereby enhancing capacitive-controlled Li-storage even at high rates. In a cathode half-cell, the free-standing film helps to provide the three-dimensional ionic and electronic movement for high rate capability and enables the delivery of good electrochemical performances. Furthermore, the assembled hybrid device LIC shows high energy density (206 Wh kg^{-1}) and high power density (7560 W kg^{-1}), with a realistic capacity retention of about 75% after 10 000 cycles. These findings contribute to advancing LICs toward practical applications, bridging the gap between energy and power density while offering an innovative solution to mitigate global LIB waste.

Conflicts of interest

The authors declare no known competing financial, academic, personal, or commercial conflicts of interest.

Data availability

The data that support the findings of this study are available from the corresponding author upon reasonable request.

Physical characteristics data of mCO-R; BJH pore size distribution plot, specific capacitances of CF-AGO-R; *b*-value calculation plots for mCO-R electrode; mass ratio optimization, voltage range optimizations, capacitance, energy, power calculations of whole LIC cell, comparison table of LIC performances. See DOI: **https://doi.org/10.1039/d5su00413f**.

Acknowledgements

SKM acknowledges the DST-IISc Energy Storage Platform on Supercapacitors and Power Dense Devices through the MECSP-2K17 program under grant no. DST/TMD/MECSP/2K17/20, Government of India, for financial support to this work. SB acknowledges the Ministry of Education, Govt of India, for fellowships. We thank the FESEM facility (under the DST-FIST project (SR/FST/ETI421/2016)) and the MSME Department, IIT Hyderabad, for their support. We thank Professor Sunil Kumar Maity, Department of Chemical Engineering, IIT Hyderabad, for BET support.

References

1 M. Chen, X. Ma, B. Chen, R. Arsenault, P. Karlson, N. Simon and Y. Wang, *Joule*, 2019, **3**, 2622–2646.
2 S. Zhao, W. He and G. Li, in *Recycling of Spent Lithium-Ion Batteries: Processing Methods and Environmental Impacts*, ed. L. An, Springer International Publishing, Cham, 2019, pp. 1–26.
3 *Recycled lithium batteries market to hit $6 billion by 2030—report*, **https://www.mining.com/recycled-lithium-batteries-market-to-hit-6-billion-by-2030-report/**, accessed January 4, 2025.
4 W. Lv, X. Zheng, L. Li, H. Cao, Y. Zhang, R. Chen, H. Ou, F. Kang and Z. Sun, *Front. Chem. Sci. Eng.*, 2021, **15**, 1243–1256.
5 G. Mishra, R. Jha, A. Meshram and K. K. Singh, *J. Environ. Chem. Eng.*, 2022, **10**, 108534.
6 T. Tawonezvi, M. Nomnqa, L. Petrik and B. J. Bladergroen, *Energies*, 2023, **16**, 1365.
7 P. Gao, P. Yuan, T. Yue, X. Zhao and B. Shen, *J. Energy Storage*, 2023, **68**, 107652.
8 Z. Zhu and X. Gao, *Adv. Sustainable Syst.*, 2025, **9**, 2400610.
9 J. Zhang, D. Chen, J. Jiao, W. Zeng and S. Mu, *Green Energy Environ.*, 2025, **10**(7), 1461–1480.
10 L. Lv, S. Zhou, C. Liu, Y. Sun, J. Zhang, C. Bu, J. Meng and Y. Huang, *Molecules*, 2024, **29**, 3161.
11 E. Paone, M. Miceli, A. Malara, G. Ye, E. Mousa, E. Bontempi, P. Frontera and F. Mauriello, *ACS Sustainable Chem. Eng.*, 2022, **10**, 2275–2281.
12 J. C.-Y. Jung, P.-C. Sui and J. Zhang, *J. Energy Storage*, 2021, **35**, 102217.
13 X. Zhu, M. Gong, R. Mo, S. Luo, J. Chen, X. Ren, X. Yan, Z. Long and S. Yang, *J. Energy Storage*, 2024, **99**, 113308.
14 X. Li, F. Dogan, Y. Lu, C. Antunes, Y. Shi, A. Burrell and C. Ban, *Adv. Sustainable Syst.*, 2020, **4**, 2000073.
15 T. Yang, Y. Lu, L. Li, D. Ge, H. Yang, W. Leng, H. Zhou, X. Han, N. Schmidt, M. Ellis and Z. Li, *Adv. Sustainable Syst.*, 2020, **4**, 1900088.
16 H. Zhao, H. Zuo, J. Wang and S. Jiao, *J. Energy Storage*, 2024, **98**, 113125.
17 P. Cattaneo, D. Callegari, D. Merli, C. Tealdi, D. Vadivel, C. Milanese, V. Kapelyushko, F. D'Aprile and E. Quartarone, *Adv. Sustainable Syst.*, 2023, **7**, 2300161.
18 S. Natarajan, M. Akshay and V. Aravindan, *Adv. Sustainable Syst.*, 2022, **6**, 2100432.
19 S. Porporato, H. Darjazi, M. Gastaldi, A. Piovano, A. Perez, B. Yécora, A. Fina, G. Meligrana, G. A. Elia and C. Gerbaldi, *Adv. Sustainable Syst.*, 2025, **9**, 2400569.
20 Y. Luo, F. Xu, L. Sun, Y. Xia, Y. Yao, Y. Guan, S. Fang, H. Hu, C. Zhang, R. Cheng, Y. Zhu, Q. Shao, Y. Zou, B. Shi and R. Li, *J. Energy Storage*, 2024, **85**, 111067.
21 S. Ghosh, M. Bhar, U. Bhattacharjee, K. P. Yalamanchili, S. Krishnamurthy and S. K. Martha, *J. Mater. Chem. A*, 2024, **12**, 11362–11377.
22 K. Serbara Bejigo, K. Bhunia, J. Kim, C. Lee, S. Back and S.-J. Kim, *J. Energy Chem.*, 2023, **82**, 148–157.
23 U. Bhattacharjee, S. Bhowmik, S. Ghosh and S. K. Martha, *Sustainable Energy Fuels*, 2023, **7**, 2321–2338.
24 S. Barcellona and L. Piegari, *J. Power Sources*, 2017, **342**, 241–251.
25 M. Goswami, S. Kumar, H. Siddiqui, V. Chauhan, N. Singh, N. Sathish, M. Ashiq and S. Kumar, in *Emerging Trends in Energy Storage Systems and Industrial Applications*, ed. Prabhansu and N. Kumar, Academic Press, 2023, pp. 223–258.
26 H. Wang, C. Zhu, D. Chao, Q. Yan and H. J. Fan, *Adv. Mater.*, 2017, **29**, 1702093.
27 *Hybrid capacitors combine technologies to get the best of both worlds*, **https://www.electronicspecifier.com/products/power/hybrid-capacitors-combine-technologies-to-get-the-best-of-both-worlds**, accessed December 12, 2024.
28 B. Li, J. Zheng, H. Zhang, L. Jin, D. Yang, H. Lv, C. Shen, A. Shellikeri, Y. Zheng, R. Gong, J. P. Zheng and C. Zhang, *Adv. Mater.*, 2018, **30**, 1705670.
29 J. J. Lamb and O. S. Burheim, *Energies*, 2021, **14**, 979.
30 P. Han, G. Xu, X. Han, J. Zhao, X. Zhou and G. Cui, *Adv. Energy Mater.*, 2018, **8**, 1801243.
31 B. Li, H. Zhang, D. Wang, H. Lv and C. Zhang, *RSC Adv.*, 2017, **7**, 37923–37928.
32 R. Lu, X. Ren, C. Wang, C. Zhan, D. Nan, R. Lv, W. Shen, F. Kang and Z.-H. Huang, *Materials*, 2020, **14**, 122.
33 M. Dwiyaniti, L. Krisnawati, A. E. Pramono, A. Subhan, R. Setiabudy, C. Hudaya, M. Dwiyaniti, L. Krisnawati, A. E. Pramono, A. Subhan, R. Setiabudy and C. Hudaya, *J. Appl. Res. Technol.*, 2023, **21**, 571–580.
34 J. Baek, S. Suh, H. Kim, H. Park, S. Kumar, T. Tamulevičius, S. Tamulevičius and H.-J. Kim, *J. Ind. Eng. Chem.*, 2023, **126**, 204–213.
35 J. Ji, S. Park and J. H. Choi, *ACS Omega*, 2023, **8**, 16833–16841.
36 S. Bhowmik, U. Bhattacharjee and S. K. Martha, *Electrochim. Acta*, 2024, **484**, 143995.
37 A. C. Lokhande, T. Hussain, A. R. Shelke, P. T. Babar, J. H. Kim and D. Choi, *J. Energy Storage*, 2022, **50**, 104251.
38 S. Dong, X. Wang, L. Shen, H. Li, J. Wang, P. Nie, J. Wang and X. Zhang, *J. Electroanal. Chem.*, 2015, **757**, 1–7.
39 J. Hao, J. Bai, X. Wang, Y. Wang, Q. Guo, Y. Yang, J. Zhao, C. Chi and Y. Li, *Nanoscale Adv.*, 2021, **3**, 738–746.
40 F. Liu, T. Yu, J. Qin, L. Zhang, F. Zhou, X. Zhang, Y. Ma, F. Li and Z.-S. Wu, *J. Mater. Chem. A*, 2024, **12**, 17327–17337.
41 S. Li, J. Zhang, H. Chao, X. Tan, X. Wu, S. He, H. Liu and M. Wu, *J. Alloys Compd.*, 2022, **918**, 165726.
42 Q. Xia, H. Yang, M. Wang, M. Yang, Q. Guo, L. Wan, H. Xia and Y. Yu, *Adv. Energy Mater.*, 2017, **7**, 1701336.
43 H. Zhu, J. Li, D. Wu, G. Zhang, Y. Sun, A. Wang and K. Sun, *Biochar*, 2023, **5**, 46.
44 M. M. Abdelaal, H.-H. Hsu, W.-L. Liao, S. G. Mohamed, C.-C. Yang and T.-F. Hung, *J. Taiwan Inst. Chem. Eng.*, 2024, **154**, 104912.
45 Z. Ding, V. Trouillet and S. Dsoke, *J. Electrochem. Soc.*, 2019, **166**, A1004.
46 M. Jerigová, M. Odziomek and N. López-Salas, *ACS Omega*, 2022, **7**, 11544–11554.
47 M. Bhar, V. Vishwakarma, K. Yalamanchili and S. K. Martha, *J. Electrochem. Soc.*, 2023, **170**, 090507.